Assessment of turbulence models for the prediction of Bénard-Von Kármán vortex shedding behind a truncated hydrofoil in cavitation conditions

IOP Conf. Series: Earth and Environmental Science **774** (2021) 012025 doi:10.1088/1755-1315/774/1/012025

Assessment of turbulence models for the prediction of Bénard-Von Kármán vortex shedding behind a truncated hydrofoil in cavitation conditions

Jian Chen, Linlin Geng, Oscar De La Torre, and Xavier Escaler*

Universitat Politècnica de Catalunya (UPC). Av. Diagonal 647, 08028 Barcelona, Spain.

E-mail: xavier.escaler@upc.edu

Abstract. The transient cavitating flow in the wake of a hydrofoil at zero incidence angle has been simulated using a homogeneous mixture cavitation mass transfer model combined with both Reynolds Average Navier-Stokes (RANS) and Scale Resolving Simulation (SRS) turbulence models. The hydrofoil geometry corresponds to a 2D NACA 0009 with a truncated trailing edge which has already been extensively investigated in the High-Speed Cavitation Tunnel of the EPFL. The hydrodynamic conditions of interest correspond to a free stream velocity of 20 m/s ($\mathrm{Re} = 2 \cdot 10^6$) without cavitation and with two different degrees of cavitation. To improve the prediction of the vortex shedding behing the hydrofoil, the $\gamma - R_{\theta t}$ transitional boundary layer model has been coupled with the turbulence models. At cavitation-free regime, all the turbulence models with the exception of the SST and LES WALE ones have the ability to predict the experimentally measured vortex shedding frequency. Nevertheless, the results indicate that, neither the SST nor the DES-SST $\gamma - R_{\theta t}$, can predict the vortex shedding frequency increase which has been experimentally observed when cavitation occurs. In contrast, the numerical results provided by the SST $\gamma - R_{\theta t}$ and the SSTCC $\gamma - R_{\theta t}$ show the capability to predict the expected shedding frequencies for both non cavitation and cavitation conditions. Beyond all expectation, the results provided by the LES WALE seem not only to overestimate the vortex shedding frequency at cavitation free conditions but also to underestimate the frequency when the cavitation number is significantly reduced.

1. Introduction

The dynamics of the alternating vortex shedding behind a hydrofoil with a truncated trailing edge will lead to an increase of the periodic pressure fluctuation in the transverse direction, which may provoke unwanted phenomena such as structural vibrations and acoustic noise. In more severe cases, this can induce a resonance in the hydraulic system or machine [1]. Simultaneously, the high vorticity concentrated inside the shed vortex may give rise to the cavitation inception if the local pressure of the vortex center falls below the vapor saturated pressure. The development of cavitation can modify the dynamics of the flow and aggravate the pressure fluctuations, the acoustic noise and induce surface erosion [2]. Howewer, research has been mainly focused on the vortex dynamics at the cavitation free regime and the cavitation effects on the Bénard-Von Kármán vortex shedding behind the hydrofoil have been given less attention.

Due to the absolute instability in the near-wake of a bluff body, Bénard-Von Kármán vortex shedding is produced as it has been experimentally confirmed for hydrofoils with blunt trailing edges. In particular, the experiments have demonstrated that the boundary layer on the hydrofoil surface suffers a laminar-turbulent transition before reaching the trailing edge, which is the key factor determining the shedding frequency of the vortex street [3].

The turbulence models selected to simulate this phenomenon have been listed and described in Table 1. Apart from the SST turbulence model, that has been used as the reference, the rest of the models are considered to be capable of capturing the effects of laminar to turbulent boundary layer transition. For that, the $\gamma - R_{\theta t}$ transition model has been developed based on the Local Correlation-based Transition Modelling (LCTM) concept where experimental correlations have been integrated into standard convection-diffusion transport equations using local variables. However, its deficiency in combination with the unsteady RANS to resolve the smallest scales of the eddies inside the near wake with enough resolution has been overcome with the development of both the DES-SST $\gamma - R_{\theta t}$ and the LES WALE models belonging to SRS. And regarding the cavitation model, the Zwart-Gerber-Belamri has been selected for its robustness and performance [9].

Table 1. Details of the turbulence models involved in the present study.

Abbreviation	***Full name***	***Reference***	***Type***
SST	Standard Shear Stress Transport	Menter (1994) [4]	RANS
SST $\gamma - R_{\theta t}$	4-equation $\gamma - R_{\theta t}$ Transitional Shear Stress Transport	Menter et.al (2006) [5]	RANS
SSTCC $\gamma - R_{\theta t}$	$\gamma - R_{\theta t}$ Transitional Shear Stress Transport with Curvature Correction	Smirnov et.al (2009) [6]	RANS
DES-SST $\gamma - R_{\theta t}$	Detached Eddy Simulation coupled with$\gamma - R_{\theta t}$transitional Shear Stress Transport	Menter et.al (2003) [7]	SRS
LES WALE	Large Eddy Simulation with Wall-Adapting Local Eddy-viscosity	Nicoud et.al (1999) [8]	SRS

2. Governing equations

2.1. Mass and momentum conservation equations

The basic quantities of the fluid flow, e.g. velocity u_i and pressure p, are derived from the mass and momentum conservation laws, which comprise the basic governing equations of the flow dynamic behavior. The continuity and the momentum equations are expressed by:

$$\frac{\partial u_i}{\partial x_i} = \dot{m}\left(\frac{1}{\rho_V} - \frac{1}{\rho_L}\right) \tag{1}$$

$$\rho_m\left(\frac{\partial u_i}{\partial t} + \frac{\partial (u_i u_j)}{\partial x_j}\right) = \frac{\partial p}{\partial x_i} + \frac{\partial}{\partial x_j}\left[2\mu_m S_{ij} + \tau_{ij}\right],\ S_{ij} = \frac{1}{2}\left(\frac{\partial u_i}{\partial x_j} + \frac{\partial u_j}{\partial x_i}\right),\ \tau_{ij} = -\rho_m \overline{u_i'' u_j''} \tag{2}$$

where τ_{ij} is the turbulence stress tensor, μ_m and ρ_m are the mixture dynamic viscosity and density, respectively, as defined by equations 3 and 4:

$$\rho_m = \rho_V \alpha_V + \rho_L(1 - \alpha_V) \tag{3}$$

$$\mu_m = \mu_V \alpha_V + \mu_L(1 - \alpha_v) \tag{4}$$

where ρ_V and ρ_L are the vapor and liquid densities, respectively.

2.2. Cavitation mass transfer model

The mass transfer rate, $\dot{m}$, between the liquid and the vapor (Equation 5) is solved with the Zwart-Gerber-Belamri cavitation model (Equation 6):

$$\frac{\partial \rho_V \alpha_V}{\partial t} + \mathrm{div}(\rho_V \alpha_V \mathbf{u}) = \dot{m} \tag{5}$$

$$\dot{m} = \begin{cases} C_p \frac{3\alpha_V \rho_V}{R} \sqrt{\frac{2}{3}\frac{(p-p_{\mathrm{sat}})}{\rho_l}}, p > p_{\mathrm{sat}} \\ -C_d \frac{3\rho_V(1-\alpha_V)\alpha_{\mathrm{nuc}}}{R} \sqrt{\frac{2}{3}\frac{(p_{\mathrm{sat}}-p)}{\rho_l}}, p < p_{\mathrm{sat}} \end{cases} \tag{6}$$

where p_v is the saturated vapor pressure with a constant value of 2000 Pa. The constants in Equation 5 and 6 correspond to the initial value of the bubble radius, $R = 1\ \mu$m, the nucleation site of volume fraction, $\alpha_{\mathrm{nuc}} = 5 \cdot 10^{-4}$, and the empirical condensation and vaporization coefficients, $C_d = 0.01$ and $C_p = 50.0$, respectively.

2.3. Turbulence models

The turbulence models mathematically described in the following subsections have been used in the present work. The SST model is mainly served as the baseline model for its popularity and robustness. Furthermore, the $\gamma - Re_\theta$ transition model renders the standard SST models capable of modeling the laminar-turbulent boundary layer transition.

SST

For the standard SST model, the turbulence kinetic energy, k, and dissipation rate, ω, are given by:

$$\frac{\partial(\rho k)}{\partial t} + \frac{\partial(\rho u_j k)}{\partial x_j} = P - \beta^* \rho \omega k + \frac{\partial}{\partial x_j}[(\mu + \sigma_k \mu_t)\frac{\partial k}{\partial x_j}], \tag{7}$$

$$\frac{\partial(\rho \omega)}{\partial t} + \frac{\partial(\rho u_j \omega)}{\partial x_j} = \frac{\gamma}{\nu_t} P - \beta \rho \omega^2 + \frac{\partial}{\partial x_j}[(\mu + \sigma_\omega \mu_t)\frac{\partial \omega}{\partial x_j}] + 2(1 - F_1)\frac{\rho \sigma_{\omega 2}}{\omega}\frac{\partial k}{\partial x_j}\frac{\partial \omega}{\partial x_j} \tag{8}$$

And the eddy viscosity is calculated by:

$$\mu_t = \frac{\rho a_1 k}{max(a_1 \omega, \Omega F_2)} \tag{9}$$

where the values of the empirical factors β^*, σ_k, σ_ω, $\sigma_{\omega 2}$, a_1 and the definition of the blending functions F_1 and F_2 can be found in [10].

SSTCC

To account for the rotation or curvature in the turbulent flow, the SSTCC model includes the empirical factor f_{r1} to correct the turbulence production P. Here, the correction is expressed by:

$$f_{r1} = \max[\min(f_{\mathrm{rotation}}, 1.25), 0.0] \tag{10}$$

$$f_{\mathrm{rotation}} = (1 + c_{r1})\frac{2r^*}{1+r^*}[1 - c_{r3}\tan^{-1}(c_{r2}\hat{r})] - c_{r1} \tag{11}$$

where the specific definition of the variables r^* and $\hat{r}$, accounting for the rotation or curvature can be found in [10]. The values of the empirical coefficients c_{r1}, c_{r2} and c_{r3} are 1.0, 2.0 and 1.0, respectively.

DES-SST

The main purpose of the DES-SST turbulence model is to implement a hybrid formula which can switch between the SST model and the LES model based on the local turbulence scales l_{DES}. The information related to the blending function F_1 can found in [10].

$$l_{DES} = \min(l_{SST}, l_{DES});\ l_{SST} = \frac{k^{\frac{1}{2}}}{\beta^* \omega}, l_{DES} = C_s \Delta \tag{12}$$

$$C_s = F_1 C_{DES}^{k-\omega} + (1 - F_1) C_{DES}^{k-e},\ C_{DES}^{k-\omega} = 0.61, C_{DES}^{k-e} = 0.78 \tag{13}$$

LES WALE

In the LES WALE, the sub-scale grid stress is modeled by the turbulent viscosity μ_t, which is given by:

$$\mu_t = \rho L_S^2 \frac{\left(s_{ij}^d s_{ij}^d\right)^{3/2}}{\left(\widetilde{s_{ij}s_{ij}}\right)^{5/2} + \left(s_{ij}^d s_{ij}^d\right)^{53/4}} \tag{14}$$

where L_s and S_{ij}^d are defined by:

$$L_s = \min(kd, C_s\Delta), S_{ij}^d = \frac{1}{2}\left(\widetilde{g_{ij}}^2 + \widetilde{g_{ji}}^2\right) - \frac{1}{3}\delta_{ij}\widetilde{g_{kk}}^2, \widetilde{g_{ji}} = \frac{\partial \widetilde{u_i}}{\partial x_j} \tag{15}$$

The length scale, L_s, can provide extra wall damping for the eddy viscosity when the flow is in the laminar state and overcome its overestimation withe the Smagorinsky model.

Coupling with the $\gamma - Re_\theta$ transition model

To account for the boundary layer transition from laminar to turbulent conditions, the LCTM was firstly implemented by Menter [5], who coupled the $\gamma - Re_\theta$ equation with the standard SST turbulence model. This method was based on the analogy with the empirical integral boundary thickness formula for boundary layer laminar–turbulent transition obtained from the experimental observations. The corresponding expressions are indicated with Equation 16 and 17:

$$\frac{\partial(\rho\gamma)}{\partial t} + \frac{\partial(\rho u_j \gamma)}{\partial x_j} = P_\gamma - E_\gamma + \frac{\partial}{\partial x_j}\left[(\mu + \frac{\mu_t}{\sigma_f})\frac{\partial \gamma}{\partial x_j}\right] \tag{16}$$

$$\frac{\partial(\rho \hat{Re}_{\theta t})}{\partial t} + \frac{\partial(\rho u_j \hat{Re}_{\theta t})}{\partial x_j} = P_{\theta t} + \frac{\partial}{\partial x_j}\left[\sigma_{\theta t}(\mu + \mu_t)\frac{\partial \hat{Re}_{\theta t}}{\partial x_j}\right] \tag{17}$$

where the intermittency, γ, is the state of the fluid flow which is 1 for the fully turbulent flow and Re_θ is the momentum-thickness Reynolds number which can be correlated with the laminar-turbulent transition onset Reynolds number. Additional specific information about the turbulence models mentioned above can be found in [10].

3. Grid and numerical setup

The experimental tests with the truncated NACA 0009 hydrofoil were carried out at the EPFL High-Speed Cavitation Tunnel within a rectangular test section of $150 \times 150 \times 750$ mm^3 as detailed in [3]. Assuming that the spanwise flow effects are negligible compared to the streamwise ones, a 2D computational domain has been considered as shown in Figure 1. The inlet boundary surface has been located at 2 times the hydrofoil chord length, C=100 mm, upstream the hydrofoil leading edge. The outlet boundary has been located at $4C$ downstream the trailing edge. The height of the fluid domain has been $1.5C$. A summary of the boundary conditions for the numerical simulation is given in Table 2. A uniform inflow of 20 m/s has been imposed at the inlet boundary. Moreover, a constant pressure has been applied to the outlet boundary to reproduce the cavitation conditions based on the ratio between the Sigma value and the incipient Sigma value, σ/σ_i, taken specifically as 1.3 for the free cavitation regime and 0.6 and 0.4 for the two cavitation regimes.

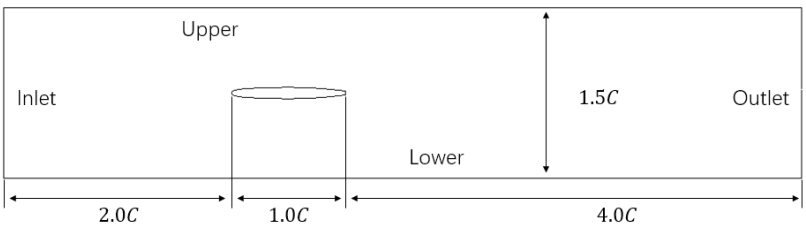

Figure 1. Computational domain of the tunnel test section with the NACA 0009 hydrofoil.

Table 2. Boundary conditions of the numerical set-up.

Boundary	***Velocity***	***Pressure***	***Turbulent energy k***	***Dissipation ε***
Inlet	Fixed value	ZeroGradie	Fixed value	Fixed value
Outlet	ZeroGradie	Fixed value	ZeroGradient	ZeroGradie

Foil	No-slip	ZeroGradie	Wall function	Wall
Upper	No-slip	ZeroGradie	Wall function	Wall
Lower	No-slip	ZeroGradie	Wall function	Wall

4. Results and discussion

4.1. Mesh convergence analysis

The Grid Convergence Index (GCI) method [11] was used to evaluate the CFD discretization error in cavitation free conditions with the SST $\gamma - R_{\theta t}$ model. For that, different meshes indicated in Table 3 were checked. The number of elements was increased progressively from mesh MC, MM, MF_1, MF_2 and MF_3 up to around 600k elements.

Table 3. Mesh number of elements, maximum y+ value, predicted shedding frequency, and percent deviation relative to the experimental result.

Mesh name	***MC***	***MM***	***MF_1***	***MF_2***	***MF_3***
Elements	80860	175616	595100	585600	605600
$y^+{}_{max}$	2.4	2.4	2.4	7.0	0.25
Shedding frequency [Hz]	1397	1512	1473	1460	1473
Percent deviation [%]	2.0	6.1	3.4	2.5	3.4

Table 4 lists the obtained results following the calculation procedures exposed in [11] for the three first meshes. It can be seen that the mesh refinement ratios r_{21} and r_{32} are both greater than 1.3 which meets the GCI analysis requirements. The quantity ϕ selected here was the vortex shedding frequency. Figure 2 (a) shows the time history of the lift coefficient, C_L, for the different meshes, and the vortex shedding frequency calculated from it and indicated in Table 2. The results show that the extrapolated value ϕ_{ext}^{21} is equal to 1461, the approximated relative error e_{a}^{21} is 2.64%, the extrapolated relative error e_{ext}^{21} is only 0.82%, and the fine-grid convergence index $\text{GCI}_{\text{fine}}^{21}$ is 1.01%. The numerical uncertainty in the fine-grid solution for the shedding frequency is about 1.01%.

Table 4. Results of the calculations to check the mesh converge analysis

N_1, N_2, N_3	r_{21}	r_{32}	ϕ_1	ϕ_2	ϕ_3	p	ϕ_{ext}^{21}	e_a^{21}	e_{ext}^{21}	GCI_{fine}^{21}
83.8k, 175k, 595k	1.84	1.47	1397	1512	1473	2.38	1461	2.64 %	0.82 %	1.01 %

Besides, two additional meshes, MF_2 and MF_3, with different first layer heights, y^+, were checked to investigate the effects on the vortex shedding frequency. The time histories of C_L for different y^+ have been plotted in Figure 2b and the corresponding vortex shedding frequencies have been listed in Table 3. The results indicate that the deviations of the numerical results with the maximum of y^+ ranging from 0.25 to 7.0 are small and limited. Also, there are no differences in the predictions of the unsteady behavior of the vortex shedding when the maximum of $y^+$is less than 2.4. Therefore, the so-called mesh MF_1 was finally selected and used in the present paper for further calculations.

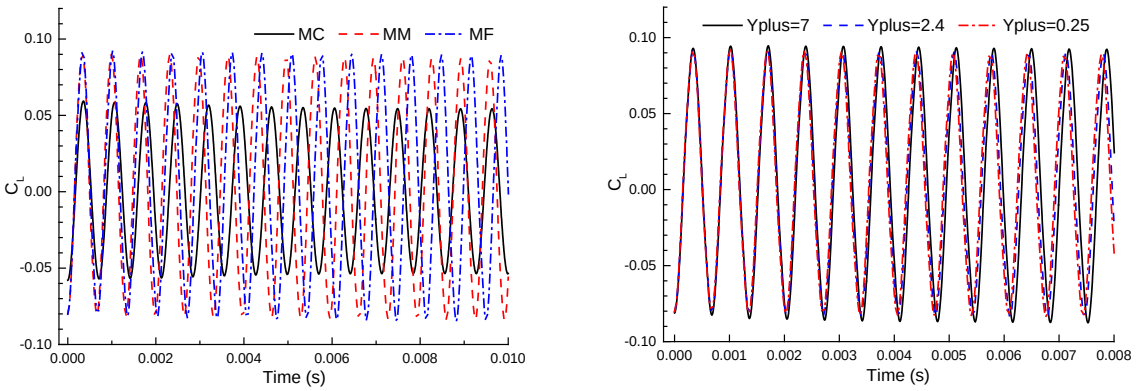

Figure 2. Time history of C_L as a function of (a) the mesh resolution and (b) the maximum y^+.

4.2. Time step independence analysis

A comparison of the C_L evolution with different time steps is shown in Figure 3. Over 12 vortex shedding cycles, the differences between results obtained with a time step of $5 \cdot 10^{-6} s$ and $1 \cdot 10^{-5} s$ are negligible, which suggests that they are independent of the time step if it falls below $1 \cdot 10^{-5} s$. Therefore, the time step in the current numerical simulations was fixed to $5 \cdot 10^{-6} s$.

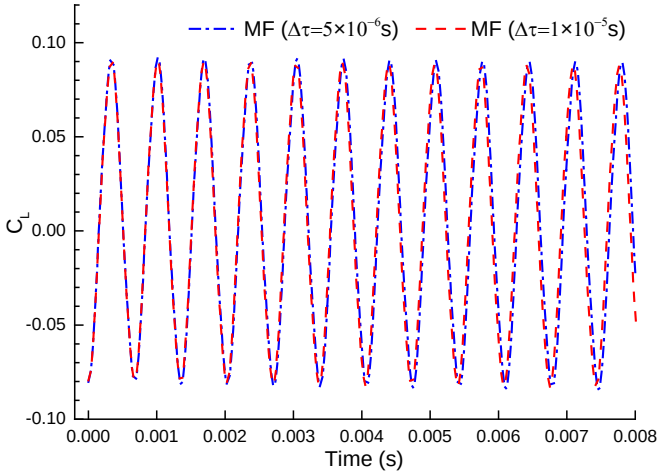

Figure 3. Time history of C_L as a function of the time step.

4.3. Cavitating vortex shedding frequency analysis

A comparison of the C_L evolutions for the different turbulence models at the three flow conditions corresponding to free cavitation regime, $\sigma/\sigma_i = 1.3$, low degree of cavitation regime, $\sigma/\sigma_i = 0.6$, and a high degree of cavitation regime, $\sigma/\sigma_i = 0.4$, are shown in Figure 4. It is observed that, with the development of cavitation, the amplitude of C_L decreases with all the turbulence models.

The amplitude of C_L predicted by the SST model under the non-cavitation condition is significantly lower than the amplitudes obtained with the other turbulence models. This is due to the fact that the laminar-turbulent transition cannot be captured by the SST turbulence model, which in turn provokes an incorrect prediction of the pressure distribution.

The vortex shedding frequencies extracted from the time histories of C_L are listed in Table 5 for all the models. The results obtained with the SST $\gamma - Re_\theta$, the SSTCC$\gamma - Re_\theta$ and the DES-SST $\gamma - Re_\theta$ show a good agreement with the experimentally measured frequency at the free cavitation regime of about 1425 Hz. Meanwhile, the SST underestimates the vortex shedding frequency and the LES WALE overestimates the frequency.

Regarding the cavitation occurrence, only the vortex shedding frequencies provided by the SST $\gamma - Re_\theta$ and the SSTCC $\gamma - Re_\theta$ show the frequency increase experimentally observed with cavitation development. On the contrary, the frequencies predicted with the SST and the DES-SST $\gamma - Re_\theta$ remain constant and no significant change is observed. For the LES WALE model, it is surprising that the vortex shedding frequency at lower cavitation numbers seems to decrease instead of increase, which can not be explained.

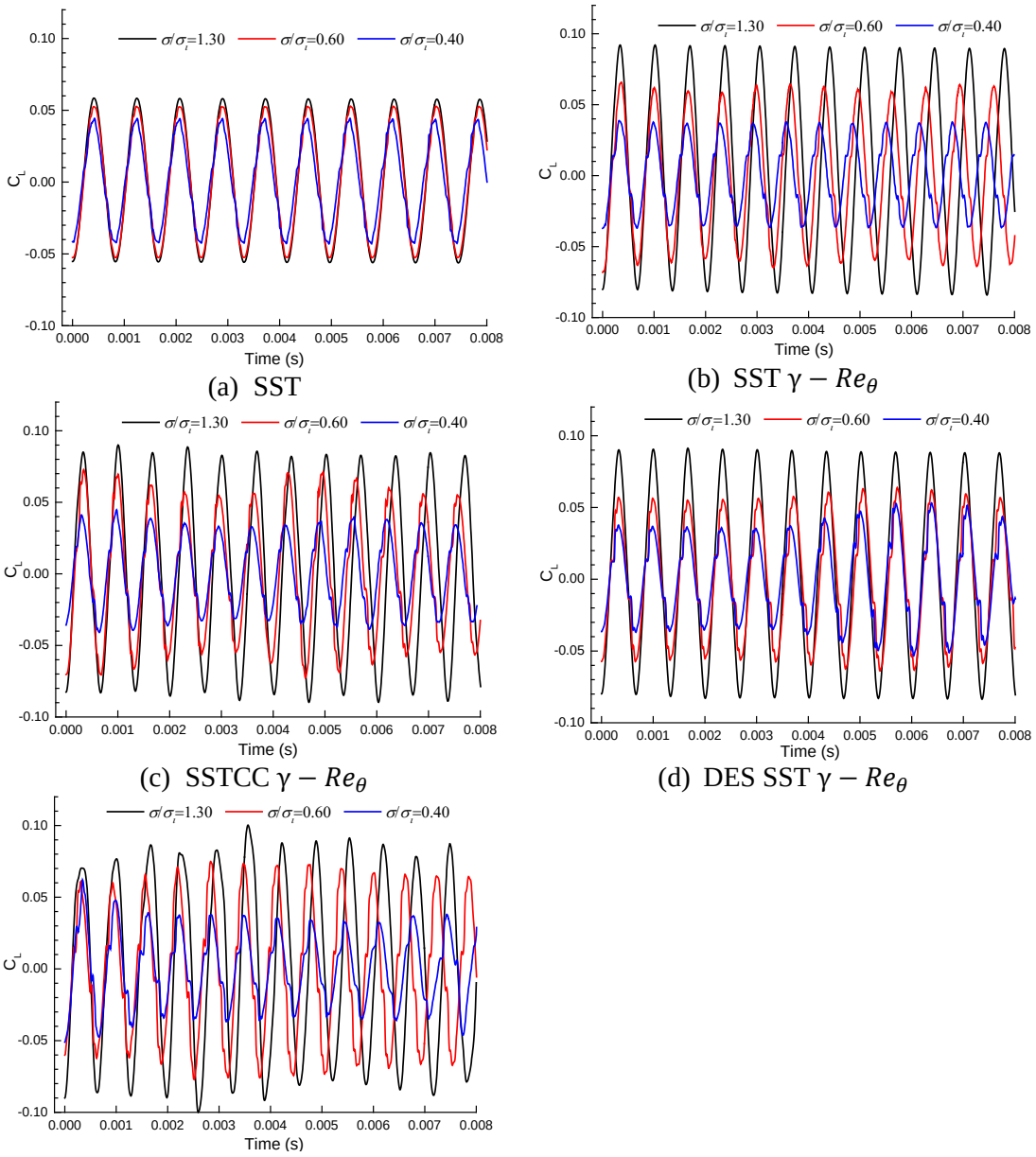

(a) SST (b) SST $\gamma - Re_\theta$

(c) SSTCC $\gamma - Re_\theta$ (d) DES SST $\gamma - Re_\theta$

(e) LES WALE

Figure 4. Time history of C_L with different turbulence models and cavitation numbers.

Table 5. Vortex shedding frequency in Hz predicted with different turbulence models and experimentally measured ones at different cavitation conditions.

σ/σ_i	*SST*	*SST* $\gamma - Re_\theta$	*SSTCC* $\gamma - Re_\theta$	*DES-SST* $\gamma - Re_\theta$	*LES WALE*	*Experiment*
1.3	1209	1473	1492	1496	1536	1425
0.6	1211	1517	1520	1496	1572	1550
0.4	1213	1549	1526	1494	1550	1600

4.4. Cavity and vorticity distribution

A comparison of the vorticity contours with different turbulence models and cavitation regimes is shown in Figure 5. It is observed that the vorticity predicted by the SST, the SST $\gamma - Re_\theta$ and the SSTCC $\gamma - Re_\theta$ turbulence models decays faster than the vorticity predicted by the DES-SST $\gamma - Re_\theta$ and the LES WALE models. This is because the vorticity diffusion by the eddy viscosity is more significant in the URANS models than in the SRS models.

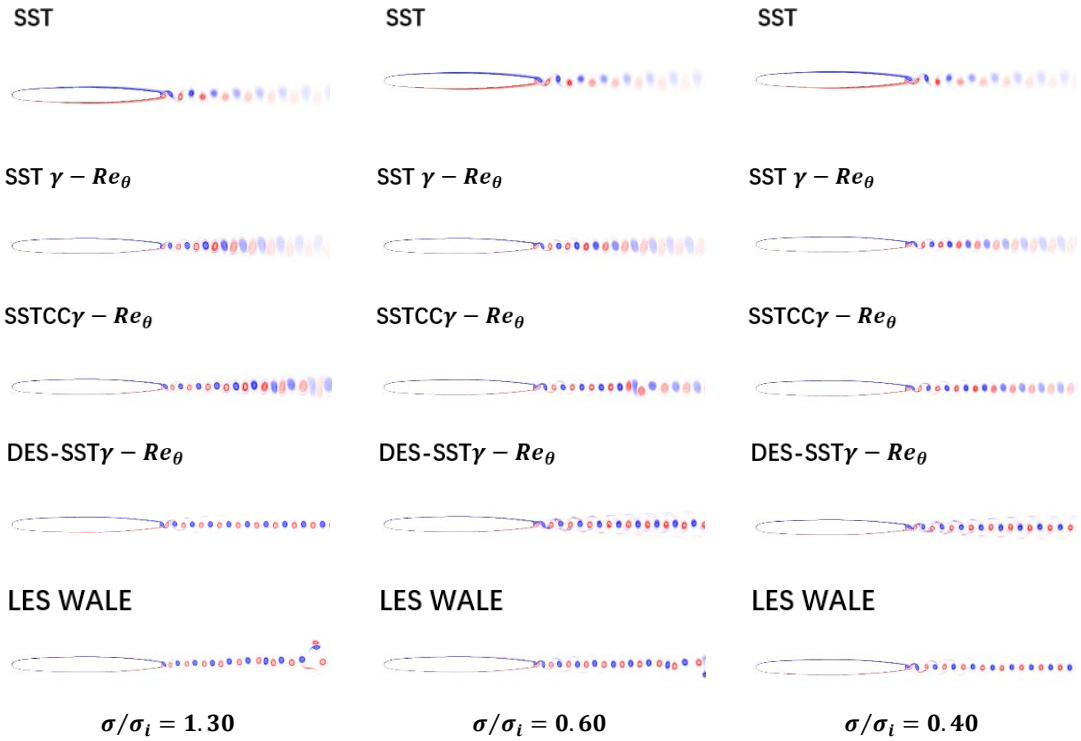

Figure 5. Vorticity contours with different turbulence models and cavitation numbers

Also, the comparison of the cavity contours with different turbulence and cavitation regimes is shown in Figure 6. For cavitation developments below σ_i, the vapor cavities appear at the rear part of the trailing edge in the wake flow. It is observed that a larger volume of vapor grows behind the trailing edge as the cavitation number is decreased. However, the vapor cavities predicted with the SST model only appear at the top and bottom vertices of the trailing edge and no vapor is present at the central axis of the hydrofoil. Nevertheless, the vapor cavities predicted by the SST $\gamma - Re_\theta$ and the SSTCC $\gamma - Re_\theta$ models also appear farther than the trailing edge at the central axis, which suggests that the cavities inside the vortices can remain more time than in comparsion with the SST model. Furthermore, the vapor cavities provided by the DES-SST$\gamma - Re_\theta$ and the LES WALE occupy almost every vortex along

the wake flow far downstream. With them, very stable vortices are observed and the vapor cavities remain in the main flow even for a longer time than with the URANS models.

Some discrepancies are observed for the change of eddy viscosity between the URANS and the SRS turbulence models. The eddy viscosity estimated with URANS is overestimated and the vortex suffers a higher viscosity diffusion than the one observed experimentally. This higher eddy viscosity will lead to the stronger diffusion of the vorticity as it is advected downstream, which will significantly reduce the vorticity strength of the vortex shedding. Therefore, the pressure inside the vortex is decreased as the vorticity decays. Once the pressure inside the vortex center is higher than the vapor saturated pressure, the vapor cavity disappears. On the other hand, the eddy viscosity estimated by the SRS is relatively smaller and thus the vapor cavity can remain more time, which is in good agreement with the experimental observations.

The mechanism for the frequency variation due to the occurence and development of the vortex cavitation has been investigated and reported in reference [12]. In this study, the identification of coherent stuctures using both Eulerian and Lagrangian methods have permitted to study the cavitation effects on the Bénar-Von Kárman vortex shedding behind the truncated hydrofoil NACA 0009. It has been found that the increase of the vortex formation length, the decrease of velocity fluctuation and the variation of the vortex morphology are the main reasons provoking the vortex shedding frequency increase with the reduction of the cavitation number.

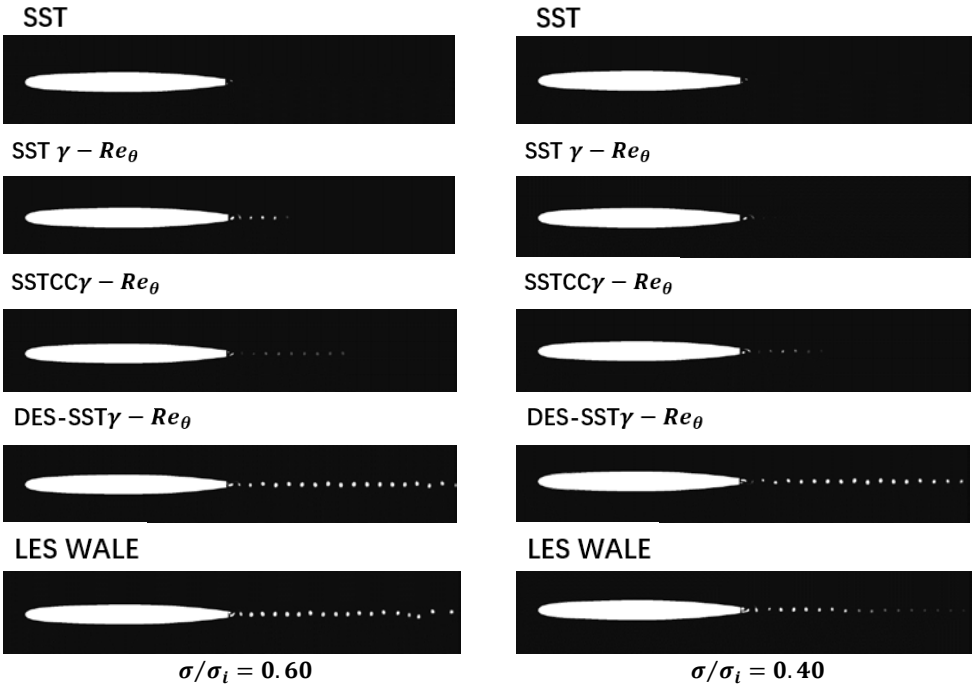

Figure 6. Vapor phase contours for different turbulence models and cavitation numbers.

5. Conclusion

The cavitating vortex shedding flow around a NACA 0009 with a truncated trailing edge has been simulated with the SST $\gamma - R_{\theta t}$, SSTCC $\gamma - R_{\theta t}$, DES-SST $\gamma - Re_\theta$, and LES WALE turbulence models. All of these models can capture the laminar-turbulent boundary layer transition phenomena that occurr on the hydrofoil upper and lower surfaces. The results obtained with the SST model have been used as reference.

For the cavitation free condition, the SST model underestimates the vortex shedding frequency because it cannot capture the laminar-turbulent boundary layer transition. The vortex shedding frequencies obtained with the turbulence models coupled with the $\gamma - R_{\theta t}$ transiton model show a good agreement with the experimental results. As cavitation appears and develops with the decrease of the cavitation number, the vortex shedding frequency increase is only predictec by the SST $\gamma - Re_\theta$ and

the SSTCC$\gamma - Re_\theta$. Meanwhile, no significant change of frequency is found with the SST and the DES-SST $\gamma - Re_\theta$ turbulence models. Last but not least, the LES WALE model not only overestimates the vortex shedding frequency at the cavitation free condition but also underestimates the frequency when the cavitation number is reduced. However, there is no explanation for these findings and it would require a further investigation.

Comparing the vapour distribution among all of the turbulence model, the results predicted with the DES-SST $\gamma - Re_\theta$ and the LES WALE models show a better agreement with experimental observations, and none of them appears to be superior to the rest.

Acknowledgments
This project has received funding from the European Union's Horizon 2020 research and innovation program under grant agreement No 814958, and from China Scholarship Council No 201808320237.

References
[1] Williamson C H. 1996 Vortex dynamics in the cylinder wake. *Annual review of fluid mechanics*, 8(1):477-539.
[2] Arndt R E A. 2002 Cavitation in vortical flows. *Annual review of fluid mechanics*, 34(1): 143-175.
[3] Ausoni P. 2009 Turbulent vortex shedding from a blunt trailing edge hydrofoil[R]. EPFL.
[4] Menter F R. 1994 Two-Equation Eddy-Viscosity Turbulence Models for Engineering Applications, *AIAA Journal*, 32,(8):1598-1605.
[5] Langtry R B, Menter F R. 2006 Correlation-Based Transition Modeling for Unstructured Parallelized Computational Fluid Dynamics Codes. *AIAA Journal*, 47(12): 2894-2906.
[6] Smirnov P E, Menter F R. 2009 Sensitization of the SST Turbulence Model to Rotation and Curvature by Applying the Spalart-Shur Correction Term. *ASME Journal of Turbomachinery*, 131, 041010.
[7] Menter F R, Kuntz M, Bender R. 2003 A scale-adaptive simulation model for turbulent flow predictions. *AIAA Paper* 2003: 0767.
[8] Nicoud F, Frédéric Ducros. 1999 Subgrid-scale stress modeling based on the square of the velocity gradient tensor. *Flow, turbulence and Combustion*, 62(3): 183-200.
[9] Zwart P J, Gerber A G, Belamri T. 2004 A two-phase flow model for predicting cavitation dynamics. *In Fifth international conference on multiphase flow* (Yokohama, Japan). 152.
[10] Menter F R. 2012 Best practice: scale-resolving simulations in ANSYS CFD. *ANSYS Germany GmbH*, 1.
[11] Stern F, Wilson R V, Coleman H W, Paterson E G. 2001 Comprehensive approach to verification and validation of CFD simulations—part 1: methodology and procedures. *J. Fluids Eng*, 123(4):793-802.
[12] Jian C, Linlin G, Xavier Escaler. Numerical Investigation of the Cavitation Effects on the Vortex Shedding from a Hydrofoil with Blunt Trailing Edge. *Fluids*, 5(4): 218-238.